Check for updates

View Article Online
View Journal

Journal of
Materials Chemistry B
Materials for biology and medicine

Accepted Manuscript

This article can be cited before page numbers have been issued, to do this please use: T. M. T. Vo, P. Sanghong, A. Pongwisuthiruchte, C. Aonbangkhen, X. Chen and P. Potiyaraj, *J. Mater. Chem. B*, 2025, DOI: 10.1039/D5TB00919G.

ROYAL SOCIETY
OF CHEMISTRY

rsc.li/materials-b

View Article Online
DOI: 10.1039/D5TB00919G

PAPER

Self-oxygenating, autonomous self-healing dual-physical crosslinked PVA/chitosan/hydrolysed collagen hydrogels for advanced wound management

Received 00th January 20xx,
Accepted 00th January 20xx

DOI: 10.1039/x0xx00000x

Tu Minh Tran Vo,[a] Patthadon Sanghong,[b] Aphiwat Pongwisuthiruchte,[a] Chanat Aonbangkhen,[b] Xiaogang Chen[c] and Pranut Potiyaraj*[a]

Impaired wound healing in diabetic patients is a significant healthcare concern, often leading to microbial infections and delayed recovery due to the absence of an optimal healing environment. An ideal wound dressing should provide self-oxygenation, self-healing properties, mechanical strength, antimicrobial activity, and biocompatibility, which are crucial factors for cell survival and tissue regeneration. This study developed a dual physically crosslinked hydrogel composed of polyvinyl alcohol (PVA), chitosan (CS), and collagen peptide (Col), incorporating polycaprolactone (PCL)-coated calcium peroxide (CPO) particles. The effects of CPO, borax, and freeze-thaw (FT) cycles on the hydrogel's physicochemical properties and biocompatibility were analyzed. CPO significantly increased dissolved oxygen levels, with 20 mg CPO per 10 g gel providing sustained oxygen release over seven days, while higher CPO concentrations led to an initial burst release. The hydrogel exhibited excellent viscoelasticity and mechanical strength, maintaining elasticity without becoming rigid. Optimizing borax content and FT cycles resulted in a self-healing hydrogel with enhanced mechanical properties. The combination of CPO and CS achieved 100% inhibition of Staphylococcus aureus, demonstrating strong synergistic antimicrobial effects. In vitro biocompatibility was assessed using an MTT assay on hydrogel extracts, revealing excellent cytocompatibility with L929 fibroblasts, with cell viability reaching 107%. Additionally, Calcein-AM/PI live/dead staining of cells cultured directly on the hydrogels confirmed sustained cell adhesion and healthy spindle-like morphology. A scratch wound assay further demonstrated enhanced fibroblast migration, achieving over 95% wound closure within three days. These findings highlight the potential of this composite hydrogel as a multifunctional wound dressing for accelerating wound healing.

1. Introduction

The management of chronic wounds presents significant clinical challenges due to the complexity of the healing process and contributing factors such as poor vascularization, persistent infection, and underlying comorbidities.[1] Infection poses a particularly critical risk, as the compromised skin barrier facilitates bacterial infiltration and colonization.[2] Therefore, effective wound management strategies must extend beyond physical coverage to include the establishment of a microenvironment that promotes key cellular processes such as proliferation, migration, and extracellular matrix (ECM) deposition.[3]

Among the various therapeutic modalities, hydrogels have emerged as promising wound dressing candidates due to their high-water content, biocompatibility, and ability to mimic the extracellular matrix of native soft tissues.[4] Natural polymers such as chitosan (CS) and collagen (Col) offer excellent biological properties, including antimicrobial activity and the promotion of tissue regeneration.[5,6] However, their limited mechanical strength restricts their practical application.[7] To address this, poly(vinyl alcohol) (PVA), a synthetic, biocompatible, and hydrophilic polymer, is frequently incorporated to reinforce the mechanical properties of composite hydrogels without compromising their biological function.[8,9]

PVA-based hydrogels can be crosslinked through either chemical or physical methods, with the freeze-thaw (FT) technique being particularly favoured due to its simplicity and absence of chemical initiators.[10] During FT cycles, water phase separation and subsequent PVA crystallization—mediated by hydrogen bonding—facilitate the formation of a robust polymer network.[11,12] In hybrid systems such as CS/PVA and Col/PVA, PVA domains form crystalline aggregates, while CS and Col chains interpenetrate and establish hydrogen bonding via their hydroxyl (-OH) and amino ($-NH_2$) groups.[13]

The design of effective wound dressings requires a delicate balance among mechanical integrity, cytocompatibility, and strong tissue adhesion. These features are often achieved by leveraging both dynamic covalent and non-covalent interactions, enabling the hydrogel to self-heal in response to mechanical disruption.[14] To further enhance gelation, sodium tetraborate (borax) has been employed to form reversible diol-borate ester bonds with polymer chains. For example, Chen *et*

---

[a] Department of Materials Science, Faculty of Science, Chulalongkorn University, Bangkok 10330 THAILAND.
[b] Center of Excellence in Natural Products Chemistry, Department of Chemistry, Faculty of Science, Chulalongkorn University, Bangkok 10330 THAILAND.
[c] Department of Materials, The University of Manchester, Manchester M13 9PL UK.
Email: pranut.p@chula.ac.th

† Electronic supplementary information (ESI) available. See DOI: 10.1039/x0xx00000x

al. demonstrated that borax-crosslinked hydrogels exhibited improved structural integrity and responsiveness when applied as dual-functional carriers in agricultural applications.[15] While these reversible borate bonds impart self-healing properties,[16] they are highly susceptible to hydrolysis in aqueous or saline environments, which compromises the long-term mechanical stability of the hydrogel network.[17] As a result, dual-crosslinking strategies that combine reversible and permanent bonding mechanisms have garnered increasing interest as a means to improve both the durability and reparability of hydrogels. However, further investigation is needed to optimize the physical crosslinking architecture—particularly in PVA/CS/Col systems—to maximize their performance in wound healing applications.

Hypoxia is a common feature of the early wound environment, primarily due to impaired local blood flow.[18] Inadequate oxygen levels inhibit cellular proliferation and migration, thereby delaying tissue regeneration.[19] Although bulk hydrogels offer structural and protective advantages, they often fall short in supplying adequate oxygen to the wound bed.[20] To address this, oxygen-releasing materials have been developed to provide localized, sustained oxygen delivery during the early stages of healing prior to neovascularization.[21]

Compared to hyperbaric oxygen therapy,[22] oxygen generated from hydrogen peroxide provides a burst release that may not be ideal for sustained therapy. In contrast, solid peroxides—especially calcium peroxide (CaO_2)—offer several advantages, including commercial availability, chemical stability, and prolonged oxygen release profiles.[23,24] For instance, CaO_2-loaded alginate hydrogels have demonstrated biphasic H_2O_2 release, yielding an initial antimicrobial effect followed by enhanced cellular proliferation.[25] Similarly, microneedle platforms incorporating CaO_2 nanoparticles have shown efficacy in penetrating biofilms and alleviating hypoxia in diabetic wounds, thereby accelerating the healing process.[26]

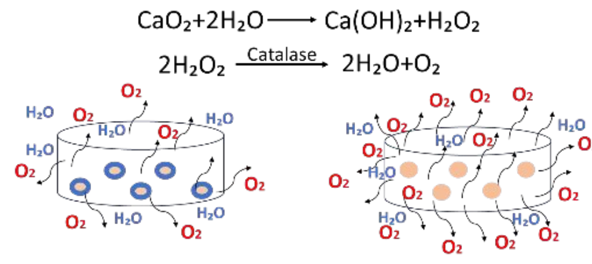

Figure 1 The difference between PCL-coated and non-PCL-coated calcium peroxide for oxygen release.

The release of oxygen from CaO_2 involves a two-step reaction: hydrolysis of CaO_2 to generate hydrogen peroxide, followed by its decomposition into oxygen in the presence of catalase.[27] However, the rapid decomposition of CaO_2 in aqueous environments limits its sustained utility. To overcome this, encapsulating CaO_2 within polycaprolactone (PCL) particles leverages the hydrophobic nature of PCL to retard water penetration, thereby modulating oxygen release kinetics.[28] As illustrated in Figure 1, this controlled interaction with water enables a more gradual and sustained release of oxygen. Additionally, solid peroxide particles can function as reinforcing agents within the polymer matrix. The incorporation of CaO_2 into PCL films slightly enhances material stiffness, as evidenced by an increase in Young's modulus, while maintaining a modulus higher than that of native skin, typically estimated at ~140 MPa.[29,30]

Despite recent advancements, the integration of oxygen-releasing functionality, self-healing capacity, and robust tissue adhesion into a single multifunctional hydrogel remains a significant challenge. In this study, we developed a multifunctional hydrogel wound dressing by incorporating PCL-coated CaO_2 (CPO) microparticles into a physically crosslinked PVA/CS/Col matrix. The composite hydrogel was synthesized through a dual-physical crosslinking strategy involving reversible borate-diol interactions and FT-induced crystallization. We systematically investigated the influence of borax content, CPO concentration, and the number of FT cycles on the hydrogel's key performance parameters, including oxygen release kinetics, mechanical strength, self-healing capacity, and tissue adhesion. Furthermore, we evaluated the biological performance of the composite hydrogels through in vitro assays assessing biocompatibility, antimicrobial efficacy, and wound healing potential, including cell proliferation and migration analyses. This work aims to establish a comprehensive design strategy for next-generation hydrogel wound dressings that simultaneously address the challenges of hypoxia, mechanical integrity, and functional recovery.

2. Experimental section

2.1. Materials

Poly(vinyl alcohol) (PVA; M_w = 145,000 g/mol and M_w = 13,000-23,000 g/mol with 90% and 89% hydrolysed, respectively) was obtained from Sigma-Aldrich (Germany). Medium molecular weight chitosan (CS; Mw = 329 kDa, degree of deacetylation = 75%) was sourced from Vietnam Food Joint Stock Company. Collagen peptides were purchased from Nippi Inc. (Japan). 75% Calcium peroxide (CAS No: 78403-22-2) was supplied from STP Chem Solutions Co., Ltd. (Thailand). Di-sodium tetraborate decahydrate (borax) 99.5 % (CAS 1303-96-4) was purchased from Q RëC™ (New Zealand). Calcein-AM/PI Living/Dead cell Double Staining Kit (CAS G1707-100T) was provided by Wuhan Koolbio Technology Co., Ltd, (Lot: MPC2505056). Trypan Blue Solution, 0.4% (CAS 15250061); Dulbecco's Modified Eagle Medium (DMEM) (CAS 11965092); Trypsin-EDTA (0.05%), phenol red (CAS 25300062); MTT (3-(4,5-Dimethylthiazol-2-yl)-2,5-Diphenyltetrazolium Bromide) (CAS M6494) were supplied by Thermo Fisher Scientific Inc.

Table 1 Formulation of CPO-entrapped PVA/CS/Col hydrogels

Sample code	CPO (mg)	5 % Borax (mL)	PVA/CS/Col solution (g)
C0B0	0	0	10
C0B0.1	0	0.1	
C10B0.1	10	0.1	
C20B0.1	20	0.1	
C40B0.1	40	0.1	
C20B0	20	0	
C20B0.05	20	0.05	
C20B0.2	20	0.2	

2.2. Fabrication of PVA/CS/Col hydrogel patch

Preparation of PCL-coated CaO_2 (CPO) microparticles. CPO microparticles were synthesized by encapsulating CaO_2 within a hydrophobic polycaprolactone (PCL) matrix following an emulsification technique.[31] An 8% (w/v) PCL solution was prepared by dissolving PCL in dichloromethane (DCM) under continuous stirring at room temperature. CaO_2 (1 g, 325 mesh) was dispersed into 100 mL of the PCL solution, which was then slowly added to an aqueous phase containing 0.5% (w/v) low molecular weight PVA while stirring at 500 rpm. The resulting emulsion was centrifuged at 1000 rpm to isolate the solid particles, which were dried under vacuum for 6 h to remove residual solvent. After drying, the CPO microparticles were sieved using a 325-mesh sieve. Morphological and elemental characterization was performed using scanning electron microscopy coupled with energy-dispersive X-ray spectroscopy (SEM-EDS). Image analysis with ImageJ software indicated that the average particle diameter was approximately 11 ± 3 μm (Figure 2a).

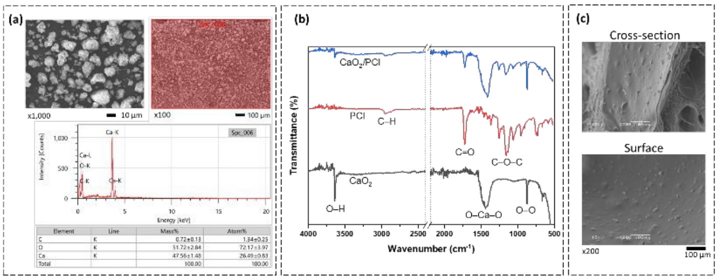

Fig. 2 (a) SEM-EDS images of CPO particles, (b) FTIR spectra of CaO_2 and CPO particles, (c) cross-sectional and surface SEM images of CPO-loaded PVA/CS/Col hydrogels.

Fabrication of dual-crosslinked PVA/CS/Col hydrogels with CPO microparticles. Hydrogels were prepared via a dual physical crosslinking strategy. CPO particles were dispersed in a 5% (w/v) PVA solution at concentrations of 0, 10, 20, or 40 mg per 10 g of gel (Phase X). Separately, a 5% (w/v) borax solution was added to a 1% CS/Col solution in volumes of 0, 0.05, 0.1, or 0.2 mL per 10 g of gel (Phase Y). Phase Y (2 g) was added dropwise to Phase X (8 g) under constant stirring, and the resulting mixture was allowed to stabilize at room temperature for 10 h. The experimental samples were coded for clarity, and their formulations are summarized in Table 1.

Subsequently, the hydrogel underwent a freeze-thaw (FT) process: freezing at –20 °C for 12 h, followed by thawing at room temperature for 12 h. This cycle was repeated up to two times, as shown schematically in Figure 3. Gelation was driven by reversible borate ester formation and crystallization of PVA domains. Detailed effects of borax content, CPO loading, and FT cycles are provided in Supplementary Table S1. The initial gelation of the hydrogel system is driven by the reversible dissociation of borax in aqueous solution into boric acid ($B(OH)_3$) and tetrahydroxyborate ions ($B(OH)_4^-$). The $B(OH)_4^-$ ions subsequently interact with vicinal diols on the polymer chains to form dynamic borate ester linkages.[32] These reversible bonds establish a physically crosslinked network that imparts self-healing capabilities to the hydrogel, enabling it to recover structural integrity following mechanical disruption. The primary aim of this study is to develop multifunctional hydrogel patches that integrate self-healing, sustained oxygen release, and enhanced mechanical properties for advanced wound care applications. Based on preliminary optimization, a single freeze-thaw (FT) cycle was selected for subsequent experimental evaluations to balance gel strength and flexibility.

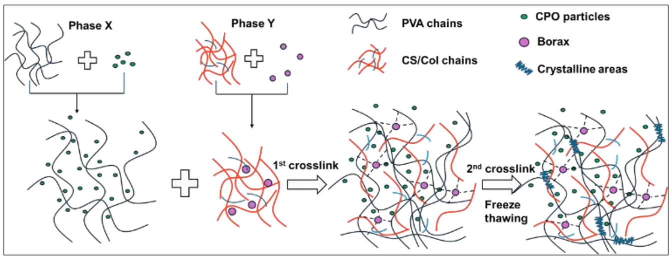

Fig. 3 Schematic illustration of the fabrication process for CPO particle-loaded PVA/CS/Col hydrogel patches.

2.3. Characterization of CPO-loaded hydrogels

Chemical structure confirmation. Attenuated Total Reflectance Fourier Transform Infrared Spectroscopy (ATR-FTIR, Nicolet™ iS50) was used to identify functional group modifications pre- and post-crosslinking. Spectra were recorded from 4000 to 500 cm^{-1} at a resolution of 4 cm^{-1} with 32 scans. Deconvolution of broad absorption bands attributed to –OH and –NH groups into Gaussian peaks was performed to analyse hydrogen bonding dynamics.

Oxygen release profile. The oxygen release kinetics of the hydrogels were evaluated using a dissolved oxygen (DO) meter. Samples were incubated in 15 mL of PBS at 37 °C, simulating physiological conditions. At defined intervals, 1 mL of the medium was extracted and analysed, then returned to maintain the solution volume. Comparisons were made among CPO-loaded hydrogels, blank hydrogels, and positive controls crosslinked solely by borax.

Water content and swelling behaviour. Water content (WC) was calculated as:

$$WC\,(\%) = \frac{m_w - m_d}{m_w} \times 100\%$$

where:

m_w = weight of the hydrogel in its fully hydrated state

m_d = weight of the hydrogel after complete drying

The swelling ratio (SR) of the hydrogel samples was determined by immersing pre-weighed dry specimens in PBS solution at room temperature until they reached their equilibrium swelling state. At each interval time, the samples were retrieved, and excess surface water was gently removed using filter paper. The swelling ratio was then calculated using the formula:

$$SR\,(\%) = \frac{m_s - m_d}{m_d} \times 100\%$$

where:

m_s = weight of the swollen hydrogel

m_d = initial dry weight of the hydrogel

The swelling behaviour of the hydrogel patches was evaluated based on Fick's fundamental law, which is commonly used to describe diffusion and swelling phenomena in

View Article Online
DOI: 10.1039/D5TB00919G

polymeric materials. The process is mathematically expressed as follows.[33]

$$F = \frac{W_t}{W_\infty} = kt^n$$

where:

W_t = the water absorbed at each interval time t

W_∞ = the amount at equilibrium

The constants k and n describe the polymer's structure and diffusion behaviour, respectively.

n ≤ 0.5: Fickian (diffusion-controlled)

0.5 < n < 1: Non-Fickian (anomalous diffusion)

To ensure precision and reproducibility, all experiments were performed in triplicate, and average values were reported.

Morphological analysis. The cross-sectional morphology of freeze-dried hydrogels was examined via scanning electron microscopy (SEM; TM3030Plus, Hitachi, Japan) following gold sputter coating.

Thermal Properties. Thermal transitions were assessed using differential scanning calorimetry (DSC; Q2000, TA Instruments, USA) from 25 to 250 °C at a rate of 10 °C/min under nitrogen flow (40 mL/min).

Viscoelastic Properties. Rheological behaviour was measured using a HAAKE MARS 40 rheometer (Thermo Fisher Scientific, Germany) with a 20-mm parallel plate setup at 25 °C. Strain sweep tests (0.01%–1000% at 1 Hz) were performed to obtain storage (G') and loss moduli (G"). Self-healing was assessed via cyclic strain testing, alternating 0.1% and 50% shear for 120 s per cycle.

Adhesion Properties. Lap shear strength of the adhesive hydrogels was assessed following a previous testing procedure with some modifications.[34] It was determined by bonding artificial skin strips (25 × 50 mm) with hydrogel adhesive on glass slides, then subjecting them to tensile loading (10 mm/min) using a universal testing machine (Lloyd Instruments, LSPlus). The maximum stress at failure was recorded; each condition was tested in triplicate.

2.4. Biological Evaluation

Cytotoxicity Assessment. The *in vitro* L929 fibroblast cell survival and viability under varying hydrogel extract conditions, characterized by different dissolved oxygen contents and crosslinker concentrations, were systematically evaluated using the MTT assay (3-(4,5-dimethylthiazol-2-yl)-2,5-diphenyltetra zolium bromide).[35] Cells (4,000 cells/well) were cultured in 96-well plates for 24 h before treatment with hydrogel extracts. Extracts were refreshed daily to simulate dynamic conditions. Viability was measured at 1, 3, and 7 days. After incubation with MTT reagent (0.5 mg/mL, 2 h), formazan was solubilized with DMSO, and absorbance was read at 570 nm using an EnSight plate reader (PerkinElmer).

Scratch Wound Healing Assay. The *in vitro* wound healing capacity was investigated via scratch assay.[36] L929 cells (4×10^4 cells/mL) were cultured in 6-well plates until 70–80% confluency. A scratch was created, and the wells were washed and imaged. Hydrogel extracts were added, and fresh medium was supplied every 24 h. Images were acquired at 0, 24, and 72 h. Wound closure was quantified using ImageJ software.

Biocompatibility tests. At the end of the wound healing assay test, the cells from each condition were detached from the bottom of the 6-well plate by adding 0.5 ml of 0.05 % trypsin and incubating the plate for 5 min at 37 °C, 5 % CO_2. The detachment process was monitored under a microscope, and after the incubation, 0.5 ml of DMEM medium was added to neutralize the trypsin. The entire cell suspension was transferred to conical tubes and centrifuged for 2 min to pellet the cells. Following centrifugation, the supernatant was discarded, and the cells were washed twice with PBS solution to remove any residual medium. The cells were then resuspended in 1 ml of DMEM medium. To assess cell viability, 10 µl of the cell suspension was mixed with an equal volume of trypan blue.[37] The resulting trypan blue/cell mixture was loaded onto a hemacytometer, and the viable cell count was recorded using the Invitrogen Countess 3 automated cell counter (ThermoFisher Scientific).

The viability of L929 cells cultured on hydrogels was assessed using Calcein-AM/PI live/dead double staining. Hydrogels were first washed three times with PBS and pre-incubated in DMEM at 37 °C for 12 hours. After removing the medium, 200 µL of L929 suspension (4×10^4 cells/mL) was seeded onto the hydrogels and cultured for 12 days. Hydrogels were washed twice with serum-free medium and incubated with a staining solution containing 2 µM Calcein-AM and 4 µM propidium iodide (PI) for 30 minutes at 37 °C. Following incubation, the staining solution was removed, and the samples were gently washed twice with PBS. Fluorescence imaging was performed using a fluorescent microscope (Axio Observer 7, ZEISS, Germany). Live cells emitted green fluorescence (Calcein-AM), while dead cells exhibited red fluorescence (PI).

Antibacterial Activity. The antibacterial activity of the hydrogels was evaluated against Staphylococcus aureus using a modified ASTM E2149-10 method.[38,39] Borax-crosslinked PVA, PVA/CS/Col, and CPO-entrapped PVA/CS/Col hydrogel beads (diameter ~10 mm) were placed individually in sterile containers and inoculated with 0.4 mL of bacterial suspension (1×10^6 CFU/mL). The samples were incubated at 37 °C in a dark environment with 90% relative humidity for 6 and 24 hours. After incubation, the bacterial suspension was collected, serially diluted in PBS, and viable bacterial counts were determined by the pour plate method on Plate Count Agar. Reduction in bacterial load was calculated as:

$$\text{Reduction}\,(\%) = \frac{B - A}{B} \times 100$$

Where:

A = log CFU/mL of viable bacteria after treatment

B = log CFU/mL of viable bacteria before treatment

Calculate antimicrobial activity by microorganisms with the following formula:

$$R = U_t - A_t$$

Where:

R = Antimicrobial activity

U_t = Average of CFU/mL after inoculation on untreated test pieces after 6 and 24 h

View Article Online
DOI: 10.1039/D5TB00919G

A_t = Average of CFU/mL after inoculation on antibacterial test pieces after 6 and 24 h

The results were expressed as mean values with standard deviations to reflect data variability, analysed using one-way ANOVA followed by Tukey HSD, conducted with Origin 2018 software. A p-value less than 0.05 was considered statistically significant.

3. Results and discussion

3.1. Characterizations of self-oxygenated and self-healing CPO-entrapped PVA/CS/Col hydrogel patches

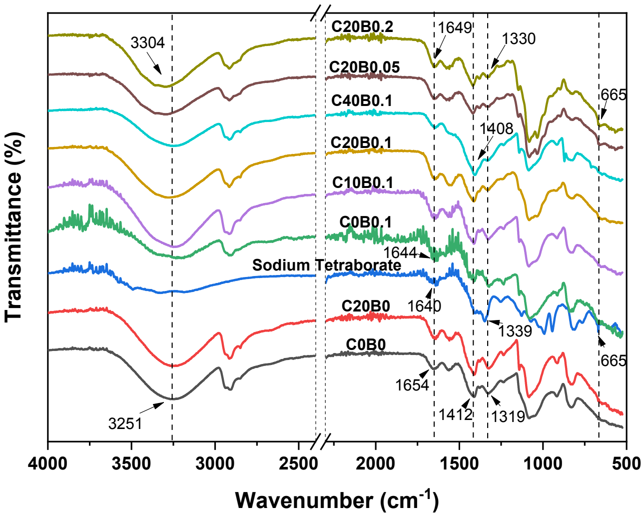

Fig. 4 FTIR spectra of PVA/CS/Col hydrogel (C0B0), CPO-loaded PVA/CS/Col without crosslinker borax (C20B0), borax-crosslinked PVA/CS/Col without CPO (C0B0.1), and dual crosslinked CPO-entrapped PVA/CS/Col hydrogel patches.

In Figure 4, the FTIR spectra of the PVA/CS/Col polymer system exhibited characteristic bands between 3000-3700 cm^{-1}, representing overlapping -OH stretching and -NH symmetrical vibrations from PVA, CS, and Col, while typical C-H stretching vibrations appeared at 2907 and 2863 cm^{-1}.[40] Absorption peaks observed at 1580 cm^{-1} and 1373 cm^{-1} were associated with the amide II and III bands, respectively in CS. Peaks at 1656, 1535, and 1240 cm^{-1} correspond to amide I, II, and III, confirming the presence of a random coil structure in Col.[41] Additionally, C-O stretching at 1062 cm^{-1} indicated contributions from alkyl groups, which was the connection between PVA/CS/Col molecules [41].

The spectra revealed Ca-O peaks of CPO particles at 1410 cm^{-1}, as shown in Figure 2b. Crosslinker borax exhibited distinct absorption at 665 cm^{-1}, corresponding to the bending vibrations of B-O-B linkages within borate networks. Upon incorporating borax molecules into the PVA/CS/Col hydrogels, the formation of complexes was confirmed by the appearance of discernible absorption peaks at 1330 cm^{-1}, attributed to the asymmetric stretching of B-O-C bonds.[42] The incorporation of borax and CPO particles into the PVA/CS/Col system results in the broadening and shifting of the -OH peak to higher wavenumbers, indicative of reduced hydrogen bonding. Borax reacts with hydroxyl groups (-OH) in PVA, CS, and Col to form borate complexes, disrupting the pre-existing hydrogen bond network. Additionally, the incorporation of CPO particles was reflected in the changes observed in the -OH stretching peak, indicating altered hydrogen bonding and structural interactions within the hydrogel matrix. The peak at 1412 cm^{-1} in the C0B0 sample was slightly shifted to 1408 cm^{-1} upon the addition of CPO, indicating subtle changes in the gel matrix. Furthermore, the intensity of this peak significantly increased with higher CPO loading, suggesting enhanced interactions or contributions from the Ca-O bonds of CPO particles within the hydrogel matrix. These changes reflect the structural and compositional impact of CPO incorporation on the PVA/CS/Col system.

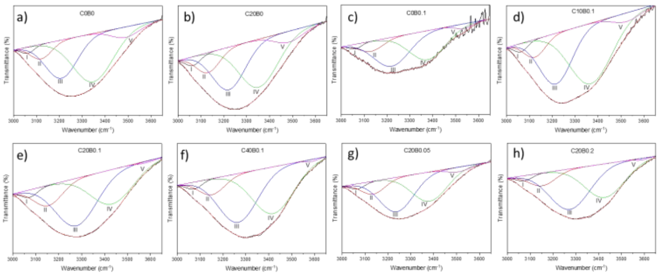

Fig. 5 Deconvolution of FTIR peaks ranging 3000 – 3650 cm-1 across hydrogel formulations: Pure PVA/CS/Col hydrogel, CPO-loaded PVA/CS/Col without crosslinker borax, and dual crosslinked PVA/CS/Col hydrogel without CPO, and Dual-crosslinked Hydrogel Patches with CPO particle entrapment

The deconvolution of FTIR peaks in the 3000-3650 cm^{-1} region for the composite materials (PVA, CS, Col, borax, and CPO) highlights distinct hydrogen bonding interactions, hydration states, and structural features, as shown in Figure 5. The 3480-3580 cm^{-1} range (Peak V) corresponds to O-H stretching vibrations from free water or weakly hydrogen-bonded water molecules,[43] while the 3350-3400 cm^{-1} range (Peak IV) reflects N-H stretching and multimer hydrogen-bonded hydroxyl groups. The 3180-3290 cm^{-1} range (Peak III) captures interconnected hydrogen bonding interactions involving both N-H and O-H groups, further emphasizing the network of hydrogen bonds within the composite and OH groups of borax. [44,45] Peaks in the 3100-3150 cm^{-1} range are associated with bound water contributions (Peak II) and weakly hydrogen-bonded hydroxyl groups. (Peak I), highlight matrix-water or matrix-matrix bonding.

The broadened peaks IV and III indicated the presence of substantial interconnected and intraconnected hydrogen bonding, which is a typical feature of hydrated polymer matrices and the interaction of crosslinker, CPO with polymers. Minor shifts in Peaks V, IV, and III, along with an intensified peak IV in C20B0 at lower wavenumbers compared to C0B0, suggest potential interactions between CPO particles and the matrix. In addition, the shifts to higher wavenumbers in the case of borax crosslinked indicate a decrease in hydrogen bonding between polymer chains, as borax forms borate complexes with hydroxyl groups, disrupting existing hydrogen bonds and forming new ester complex bonds. Peak V around 3520-3600 cm^{-1} significantly decreases when the crosslinker borax content and CPO amount rise to 0.2 ml and 40 mg, respectively, compared to composites with lower CPO or borax concentrations (10 mg and 0.05 ml). This trend indicates that higher concentrations of CPO and borax create a denser structure, reducing free water within the hydrogel matrix, which aligns with SEM images and swelling ratio results. The composite hydrogel, containing both crosslinker borax and CPO particles, showed enhanced intensity at peak III, suggesting that increased borax concentration strengthens

DOI: 10.1039/D5TB00919G

specific interactions with the matrix, potentially promoting borate complex formation.

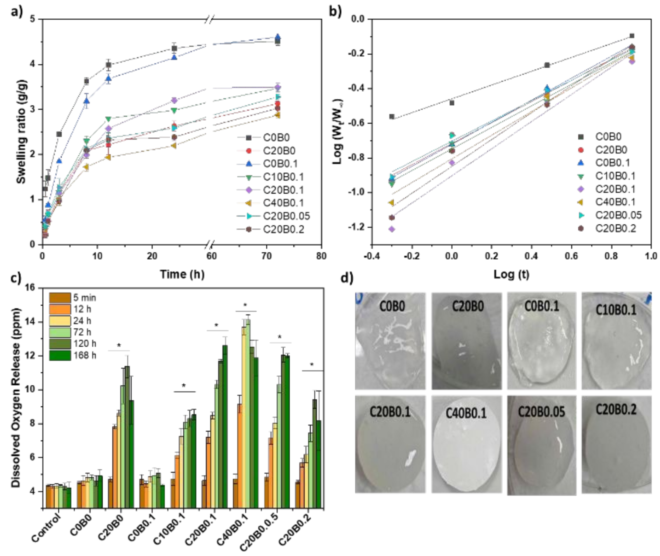

Fig. 6 (a) Swelling ratio (g/g) vs. time (h); (b) log(Wt/W∞) vs. ln(t) plot; (c) DO release profile; (d) hydrogel images: comparison among PVA/CS/Col composite hydrogels with and without crosslinker borax or CPO particles under one FT cycle, and control without hydrogel samples, with *$p < 0.05$*.

The swelling behaviour of hydrogels with varying borax concentrations and CPO loading levels is shown in Figures 6a-b. The C0B0 formulation exhibited the highest swelling ratio, which can be attributed to its loosely crosslinked network, lacking both borax-mediated crosslinks and CPO-induced reinforcement. As seen in Figure 6d, hydrogels prepared with low levels of borax and CPO appeared poorly formed, displaying limited structural integrity. With the introduction of borax, the swelling ratio increased by up to 4.5 g/g, likely due to the hydrophilic nature of borax. Its hydroxyl groups facilitate hydrogen bonding with water molecules, promoting greater water uptake and network expansion.[46] In contrast, increasing the CPO content led to a notable decrease in swelling. In particular, the swelling ratio declined significantly from 3.2 to 2.3 g/g when the CPO loading increased from 10 to 40 mg. This trend suggested that higher CPO loading restricts polymer chain mobility and reduces the available free volume for water diffusion. As presented in Table S2 (Supplementary), the swelling coefficient (n) of the composite hydrogels ranged from 0.58 to 0.78 in the presence of borax and CPO, indicating that water diffusion occurred via a non-Fickian transport mechanism. In contrast, the C0B0 sample exhibited a diffusion exponent slightly below 0.45, which suggests that the rate of water penetration was slower than the relaxation rate of the polymer chains. Under these conditions, diffusion remains the primary mechanism, and the process is still classified as Fickian.[47] Investigating the diffusion behaviour of the hydrogels, along with the enhanced structural stability achieved through increased CPO loading and borax content, is essential for ensuring the controlled release performance of the hydrogel system.

The sustained release of oxygen is crucial for regenerative medicine applications, particularly in wound healing, as it ensures a continuous oxygen supply to promote cell proliferation, migration, and overall tissue regeneration. Hydrogels were immersed in DI water and incubated at 37 °C to evaluate the oxygen release capability of hydrogel patches. The results revealed that CPO microparticles-entrapped hydrogels released significantly higher levels of dissolved oxygen (6 -14 ppm) compared to the hydrogels without CPO loading, which only released 4.5 - 5 ppm of oxygen after 24 h, as displayed in Figure 6c. The study also showed that the amount of CPO loading influenced the release profile. As the CPO concentration increased from 10 to 40 mg, oxygen release levels also increased. Hydrogels with 20 mg of CPO demonstrated a consistent and prolonged oxygen release, reaching a concentration of 12 ppm after 168 hours (7 days). This indicated a stable and sustainable release profile that could be advantageous for long-term therapeutic applications. However, hydrogels with 40 mg of CPO exhibited an initial burst release, with oxygen levels reaching 13.5 ppm after 24 h and slightly enhanced to 14 ppm after 72 h but subsequently dropping to 11 ppm after 168 h (7 days), suggesting an initial oversupply followed by depletion over time. Hydrogels with higher crosslinking density, such as C20B0.2, exhibited lower DO release compared to those with lower borax content. This is likely due to the denser network hindering the diffusion of oxygen and CPO degradation products, thereby prolonging release.

The viscoelastic properties of hydrogels were studied to establish the relationship between their mechanical strength and hydrogel network structure. Oscillatory rheological measurements confirmed both the storage modulus (G') and loss modulus (G"). Amplitude sweep experiments were conducted to determine the linear viscoelastic range (LVR), with strains ranging from 0.01 % to 1 %. Beyond the critical strain, the G' values of crosslinked PVA/CS/Col-based hydrogels with/without CPO loading decreased sharply with increasing strain, demonstrating a gel-sol transition where the hydrogels transitioned to a liquid-like state.

The incorporation of CPO and borax crosslinking significantly enhanced the mechanical properties of the hydrogels. The storage modulus (G') increased from 300 Pa in the PVA/CS/Col hydrogel (C0B0) to approximately 1500 Pa in the hydrogel crosslinked with borax and containing 20 mg of CPO (C20B0.2), as shown in Figure 7a. This improvement highlights the role of CPO particles and crosslinker borax in reinforcing the hydrogel structure. The strengthening effect became even more pronounced with higher CPO concentrations, demonstrating its ability to act as a reinforcement agent, as shown in Figure 7b. Additionally, the viscoelastic properties were influenced by the number of FT cycles applied to the hydrogels (Figure 7c). The G' value at 0.01 % strain increased fivefold, from 500 Pa to 2500 Pa, as the number of FT cycles increased from 0 to 2. However, the strain at which G' = G" decreased significantly, from 300 % strain (0 cycles) to 10 % strain (2 cycles), indicating that the FT cycles created a more rigid gel structure. This rigidity is attributed to an increase in the crystalline regions within the polymer network.[48]

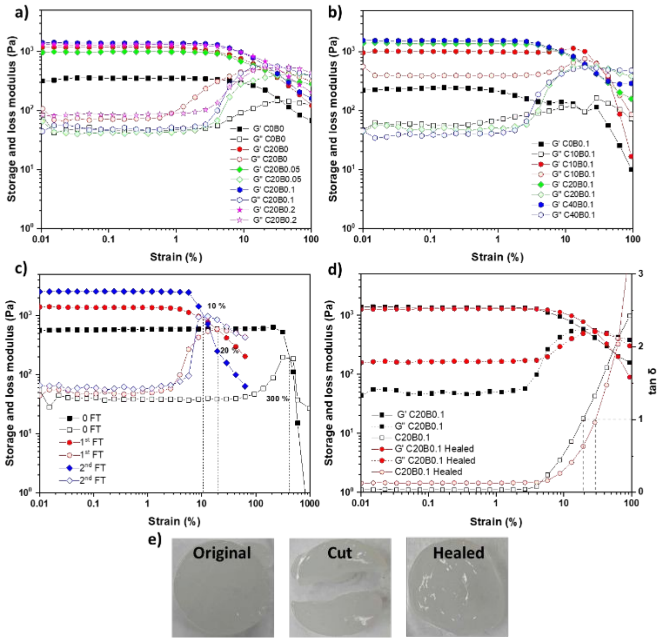

Fig. 7 (a) Strain sweep measurements of G' and G" for PVA/CS/Col hydrogels: at different concentrations of borax; (b) varying CPO loading amounts; (c) different FT cycles for C20B0.1 hydrogel; (d) the original hydrogel and the healed hydrogel post-cutting; (e) visual images of C20B0.1 hydrogel before cutting and after self-healing.

To further understand the viscoelastic behaviour of self-healing hydrogels, step-strain alternating rheology tests were performed, as shown in Figure 8a-c. The hydrogels (C20B0.1, C40B0.1, and C20B0.2) were subjected to 3 cycles of alternating low (0.01 %) and high (50 %) shear strain. When the strain increased to 50 %, G" exceeded G' value, indicating that the hydrogel network was disrupted, particularly in the case of C20B0.1. Upon reducing the strain back to 0.01 %, both G' and G" recovered to their initial values, demonstrating the self-healing ability of the hydrogel due to the reformation of hydrogen bonds[49] and dynamic borax crosslinks.[50] Moreover, the viscoelastic behaviour of C20B0.1 in its original state before cutting and after healing was also analysed in Figures 7d and 7e. After healing, G' was slightly lower than its original value, and the gel-sol transition point shifted from 10 % strain in the original state to 20 % strain post-healing. This behaviour suggests partial recovery of the mechanical properties due to the reorganization of the dynamic crosslinked network rather than the irreversible crystal part. Visual evidence confirmed that the hydrogels almost regained structural integrity after being cut, showcasing their adaptive self-healing nature.

For those hydrogels with higher CPO loading (C40B0.1) and greater borax crosslinking density (C20B0.2), their viscoelastic behaviour under strain was distinct. At 50 % strain, the storage modulus of both hydrogels decreased but remained above the loss modulus, indicating that the gels retained their solid-like structure despite partial network damage. In the case of C40B0.1, G' recovered after the first strain cycle but did not return to its original value, suggesting incomplete healing. This incomplete recovery might be due to the higher CPO content, which could interfere with the dynamic bonding necessary for full self-healing. In contrast, C20B0.2 showed a minimal reduction in G' at 50 % strain compared to C20B0.1, which can be attributed to the denser borax crosslinked network. The compact structure resisted further damage even under high strain, and the hydrogel fully recovered its original G' value after returning to 0.01 % strain for all three cycles. This indicates that the enhanced crosslink density in C20B0.2 significantly improved its resistance to strain and its ability to recover fully.

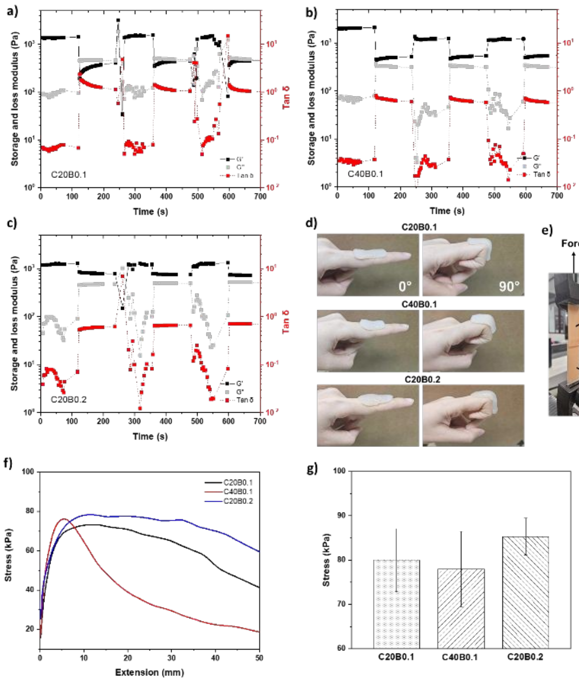

Fig. 8 (a) Time sweep measurement of C20B0.1, (b) C40B0.1, and (c) C20B0.2 under alternating 0.01 % and 50 % shear strain % to measure the self-healing property of hydrogels. Each strain interval was kept at 120 s, and the fixed frequency was kept at 1 Hz; (d) hydrogel adherence to the skin in a flat (0°) position and during a 90° bend; (e) schematic representation of a lap shear test performed with artificial skin; (f) shear force - displacement curves of dual physically crosslinked PVA/CS/Col hydrogels; (g) lap shear strength measurements for C20B0.1, C40B0.1, and C20B0.2 samples, with a minimum of three replicates per group.

The self-adhesive nature of the hydrogels is particularly beneficial for wound care applications as it enables direct and conformal attachment to the wound site. As a visual observation in Figure 8d, the hydrogel maintained intimate contact with the skin at interphalangeal joints, demonstrating its adaptability to dynamic and irregular skin surfaces. To further assess the adhesive universality of the composite hydrogels, their adhesion strength was quantified using a lap shear test, in which the hydrogel was sandwiched between two substrates (Figure 8e). The maximum shear stress at detachment was considered the interfacial adhesive strength. For the C20B0.1, C40B0.1, and C20B0.2 formulations, the measured adhesion strengths were 80, 76, and 85 kPa, respectively (Figure 8g). These results suggest that increasing the CPO content slightly reduces adhesiveness. In contrast, higher borax concentrations, contributing to more dynamic crosslinking, enhanced the lap shear strength. Furthermore, for the C40B0.1 hydrogel, initial interfacial slippage occurred at approximately 10 mm of extension. In contrast, hydrogels with lower CPO content demonstrated more stable adhesive performance, maintaining consistent shear stress up to 30 mm of extension. Even at 50 mm, only around a 20 % decrease in shear stress was observed, highlighting their superior resistance to mechanical separation and improved interfacial durability, as shown in Figure 8f.

Figure 9 illustrates the heat flow across three stages, including first heating, cooling, and second heating, each performed at 10 °C/min, revealing the thermal transitions of PVA/CS/Col hydrogels with varying CPO loading amounts and borax concentrations. During the first heating, the melting temperature (T□) of the PVA/CS/Col matrix decreased from 224 °C to 215 °C with CPO incorporation, as CPO disrupted crystalline regions and reduced thermal stability. However, dual crosslinking with borax and the freeze-thaw process enhanced T□, especially with higher CPO and borax concentrations, as summarized in Table S2 (Supplementary). This enhancement is attributed to stronger interactions between borax crosslinks and polymer chains, which act as a reinforcement factor. The ΔH (J/g) of CPO-loaded borax crosslinked hydrogels was lower than the neat polymer matrix (C0B0), indicating a reduction in crystallinity. This suggests that dual crosslinking and the incorporation of CPO disrupt the crystalline structure of the polymers.

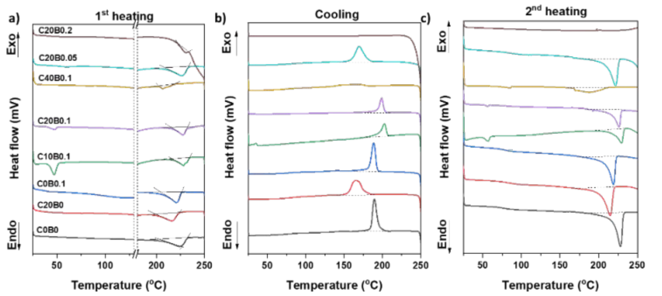

Fig. 9 DSC curves of CPO-entrapped PVA/CS/Col hydrogel patches: (a) 1st heating, (b) cooling, and (c) 2nd heating curves.

In the cooling stage,[51] the crystallization temperature (T_c) decreased from 185 °C (C0B0) to 160 °C (C20B0) due to disrupted crystallization caused by CPO. This trend became more pronounced with excessive CPO at 40 mg CPO (C40B0.1). Furthermore, no crystallization peaks (exo) and melting peaks (endo) during 2nd heating appeared in C20B0.2, indicating that after 1st heating, the crystallization was suppressed, leading to amorphous-like behavior. In contrast, lower crosslinking levels allowed partial crystallization and corresponding melting peaks in the 2nd heating curves. These results underscore the significant role of CPO and borax concentrations in regulating the thermal response and structural flexibility of PVA-based hydrogels.

The internal microstructure of the hydrogel cross-sections was analysed using SEM. As shown in Fig. 10, all the freeze-dried hydrogels exhibit a network of interconnected pores. The plate-like structures observed in the image of freeze-thawed PVA/CS/Col (C0B0) indicate the formation of a material where ice crystals served as templates during the freezing process, creating voids or layered formations. After thawing, these voids are preserved, resulting in interconnected pores or lamellar channels.[52] The microstructural changes in the composite hydrogels following the dual physical crosslinking process highlight the impact of varying CPO and borax content on porosity and water retention properties. C20C0.1 exhibited a well-connected porous structure, with smaller pore sizes as CPO loading increased than C10B0.1, enhancing crosslinking and tightening the hydrogel network. C20B0.05 displayed a less uniform interconnected structure, while denser structures were observed in C40B0.1 and C20B0.2 due to higher crosslink density, significantly reducing pore size. This increased density resulted in decreased water content and swelling ratios compared to C0B0, which had the highest water absorption capacity due to its looser polymer network, as summarized in Table S2 (Supplementary).

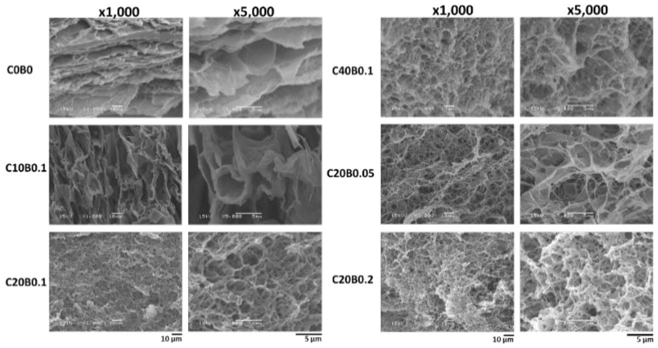

Fig. 10 Cross-sectional SEM images of PVA/CS/Col gel and its composites at x1,000 and x5,000 magnifications.

3.2 Biological evaluations of CPO-loaded PVA/CS/Col wound dressing

The biocompatibility of the hydrogels was thoroughly evaluated by utilizing L929 cells, a well-established connective tissue cell line known for its critical function in promoting wound healing.[53] To evaluate the relative proliferation of fibroblast cells in response to extracted CPO loaded-dual crosslinked PVA/CS/Col hydrogel patches with varying concentrations of CPO and crosslinker borax, MTT assays were conducted after 1, 3, and 7 days of culture and the medium was refreshed daily with hydrogel extractions, as showed in Figure 11a. The absorbance values of the MTT solution were proportional to the number of viable cells, with higher absorbance indicating greater cell survival. Results revealed that cell viability improved with increasing CPO content, peaking with C20B0.1 at 1 and 3 days.

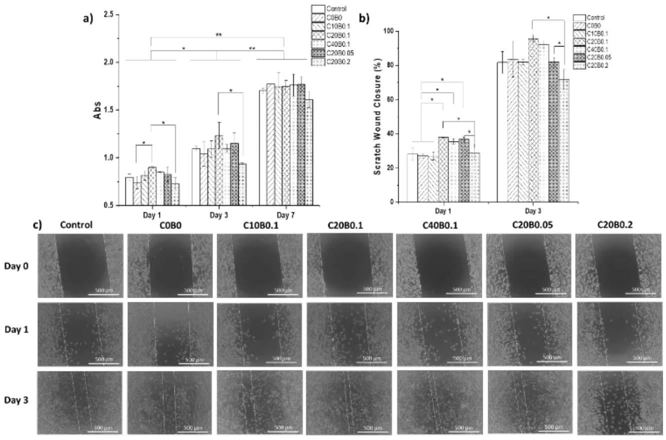

Fig. 11 (a) The absorbance of cells and formazan product using MTT assay; (b) the percentage of scratch wound closure; (c) and microscopy images of scratched areas from day 0 to day 3 of PVA/CS/Col gel and CPO-loaded PVA/CS/Col gel patches. Statistical significance is indicated by $p < 0.05$ (*) and $p < 0.01$ (**).

View Article Online
DOI: 10.1039/D5TB00919G

However, a slight reduction in viability was observed with C40B0.1, likely due to excessive CPO. By day 7, no significant differences in cell viability were noted between the hydrogel samples and the control condition without hydrogels. In contrast, C20B0.2 exhibited consistently lowest cell survival across all time points (1, 3, and 7 days), attributed to the higher release of crosslinker borax content, which might have adversely impacted cell proliferation. These findings underscore the non-toxic nature of the PVA/CS/Col composite hydrogels within certain CPO and borax concentrations, which enhanced cell growth compared to the control. This improvement is likely due to elevated dissolved oxygen levels in the culture medium, promoting cell proliferation and survival.

The efficiency of wound healing is closely tied to the migration rate of cells at the wound site.[54] To assess this target, an *in vitro* scratch assay was conducted, demonstrating the wound-healing potential of the composite hydrogels. As illustrated in Figures 11b and 11c, all hydrogel groups showed excellent affinity for L929 cells and significantly enhanced their migration compared to the control group, except for C20B0.2. After 1 day of incubation, hydrogels C20B0.05, C20B0.1, and C40B0.1 achieved approximately 38 % closure of the scratched area, surpassing 90 % closure after 3 days, indicating their potential to effectively accelerate cell migration and enhance wound healing. Furthermore, the effect of hydrogel extracts on cell viability and proliferation was validated after 3 days of the scratch wound healing assay using live/dead cell staining following trypsinization, and cells were dyed with trypan, as shown in Figure 12. Results revealed a slight improvement in the live/death ratio for the PVA/CS/Col (C0B0) and CPO-loaded hydrogels. Notably, the C20B0.1 hydrogel demonstrated 94 % cell viability, with only 6 % cell death, representing a 9 % improvement in live cell rate compared to the control. However, excessive borax concentration resulted in a reduced living cell ratio of only 65 %. These findings emphasize that optimizing CPO and crosslinker borax concentrations can significantly enhance cell viability, proliferation, and migration.

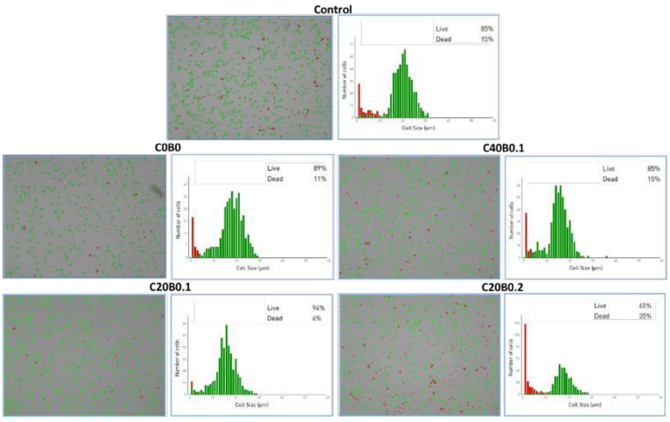

Fig. 12 Live-dead assay and cell size distribution of extracted hydrogels.

To assess the biocompatibility and cell-hydrogel interactions, L929 fibroblasts were cultured on the hydrogel, and the attachment and morphology of cells were visualized using fluorescence microscopy. Figure 13 illustrates that all hydrogel formulations supported the attachment and viability of L929 fibroblasts over a 12-day culture period, as confirmed by Calcein-AM/PI staining, though notable variations in cell behavior were observed. Among the tested samples, the C20B0.1 hydrogel created a favorable environment for cell adhesion and proliferation, demonstrated by dense cell coverage, a well-spread spindle-shaped morphology, and strong green fluorescence with minimal dead cells, indicating excellent biocompatibility.[55] These results are consistent with prior reports that highlight the critical role of hydrogel surface hydrophilicity, mechanical stiffness, and adhesive properties in regulating fibroblast attachment and proliferation.[56] In contrast, the C0B0 and C40B0.1 hydrogels exhibited a higher proportion of rounded cells with reduced elongation compared to the C20B0.1 hydrogel and the control sample. Although cell viability remained high, these results suggest that the surface properties of C0B0 and C40B0.1 hydrogels were less conducive to strong fibroblast adhesion. The introduction of CPO and borax crosslinks enhanced the adhesive capacity of the hydrogels relative to the C0B0 condition, thereby improving fibroblast attachment. This observation is consistent with the adhesive force measurements shown in Figure 8f, where the higher CPO content in C40B0.1 resulted in reduced adhesive extension. However, excessive borax content negatively impacted cell survival [57], leading to uneven cell distribution and increased red fluorescence intensity compared to the other conditions. Furthermore, previous studies have reported that hydrogels with a balanced structure, allowing adequate nutrient diffusion and stable surface properties, promote sustained fibroblast growth [58], thereby supporting cellular activities essential for tissue regeneration.

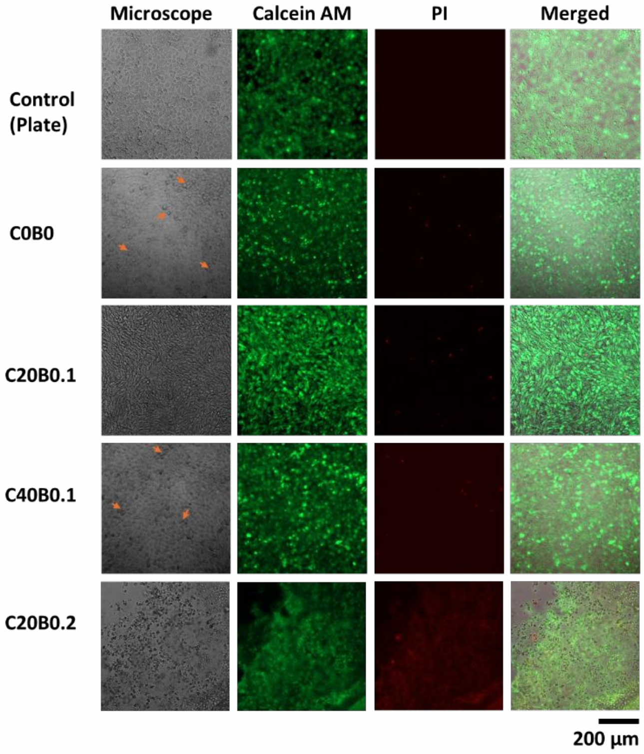

Fig. 13 (a) L929 cells cultured on hydrogels and (b) Calcein AM/PI staining images of L929 cells on CPO-entrapped PVA/CS/Col hydrogels after 12 days of culture, captured at 20× magnification.

Bacterial infections, such as those caused by *S. aureus*, are known to induce a prolonged inflammatory response that significantly disrupts the wound healing process.[59] The antibacterial performance of hydrogels C0B0, C20B0.1, and the positive control PVA gel (lacking CS, Col, and CPO) was evaluated, with the results summarized in Figure 14 and Table S3 (Supplementary). The data showed that, after 6 h, C0B0 and C20B0.1 exhibited significant reductions in S. aureus count, achieving 84 % and 100 % reductions,

View Article Online
DOI: 10.1039/D5TB00919C

respectively, compared to only a 15 % reduction with the PVA gel. Furthermore, both C0B0 and C20B0.1 achieved complete bacterial elimination (100 % reduction) after 24 h. Meanwhile, the reduction in bacterial colonies observed in the PVA control group at 24 h is likely attributed to the presence of borax, which is also known to exhibit antibacterial activity.[60] These findings demonstrate the intrinsic antibacterial activity of the dual-crosslinked PVA/CS/Col hydrogel, which is primarily attributed to the synergistic antimicrobial effects of chitosan and the borax crosslinker. Notably, the enhanced antibacterial performance of the C20B0.1 formulation further underscores its potential as a multifunctional wound dressing material, capable of both preventing bacterial infection and supporting the wound healing process.

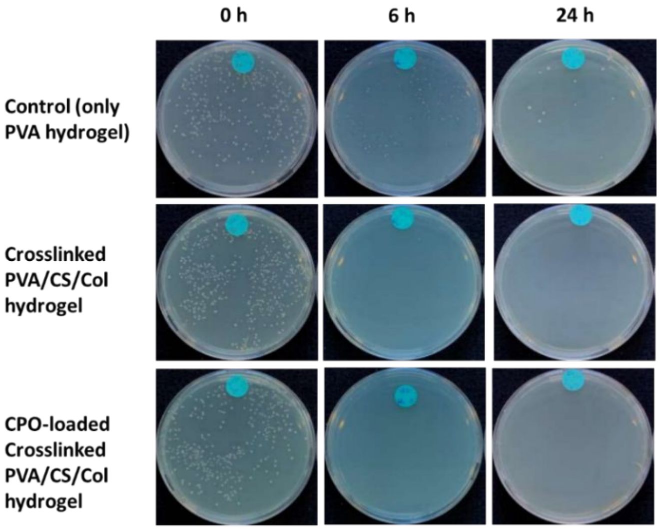

Fig. 14 The number of bacteria S. aureus in crosslinked-PVA gel (positive control), PVA/CS/Col gel, and CPO-entrapped PVA/CS/Col hydrogels at time 0 h at dilution 10^{-3} for all of the conditions, 6 h at dilution 10^{-2} for the positive control sample and at dilution 100 for other cases, and 24 h at dilution 100 for all of the samples.

4. Conclusions

Self-oxygenating and self-healing PVA/CS/Col hydrogel patches were successfully developed using a dual physical crosslinking technique. The incorporation of CPO particles enabled sustained oxygen release for up to seven days at an optimal loading of 20 mg per 10 g of gel, effectively preventing the burst release observed at higher CPO concentrations. By modifying borax content and optimizing freeze-thaw cycles, which involved an initial borax crosslinking step followed by freezing at –20°C for 12 hours and thawing at room temperature for another 12 hours, a balance between dynamic crosslinking and crystallinity was achieved. The entrapment of CPO within the polymer matrix not only acted as a reinforcement factor but also enhanced mechanical strength while preserving elasticity and preventing brittleness, ensuring adaptability to wound sites. The morphological transformation of these hydrogels evolved from a layered lattice (C0B0) to a highly interconnected porous structure with the addition of CPO particles and borax crosslinking. Additionally, the composite hydrogels exhibited outstanding antimicrobial properties, achieving 100% inhibition of *Staphylococcus aureus* within six hours. Cytotoxicity assessments using L929 fibroblasts confirmed the excellent biocompatibility of the hydrogels, with cell survival rates reaching 107% relative to the control group (without hydrogel). Furthermore, Calcein-AM/PI staining revealed dense cellular coverage and well-spread spindle-shaped fibroblasts directly adhered to the hydrogel surface, indicating favorable cell–material interactions and cytoskeletal organization. Interestingly, the hydrogel significantly accelerated wound healing, promoting cell migration and achieving over 95% wound closure within just three days. This multifunctional hydrogel integrates oxygen delivery, mechanical strength, self-healing ability, antimicrobial efficacy, and biocompatibility, making it an advanced solution for wound management. Its ability to provide an optimal healing environment underscores its potential as a highly effective wound dressing.

Authorship contributions

Tu Minh Tran Vo: conceptualization, formal analysis, investigation, methodology, visualization, and writing – original draft. Patthadon Sanghong: investigation. Aphiwat Pongwisuthiruchte: investigation. Chanat Aonbangkhen: methodology and investigation. Xiaogang Chen: Supervision. Pranut Potiyaraj: conceptualization, formal analysis, funding acquisition, methodology, resources, supervision, and writing – review & editing.

Conflicts of interest

There are no conflicts to declare.

Data availability

The data supporting this article have been included as part of the Supplementary Information.

Acknowledgements

This work was supported by The Second Century Fund (C2F), Chulalongkorn University, Thailand.

References

1 O. Krizanova, A. Penesova, A. Hokynkova, A. Pokorna, A. Samadian and P. Babula, *Int. Wound J.*, 2024, **21**, e14405.
2 H. Zhang, X. Lin, X. Cao, Y. Wang, J. Wang and Y. Zhao, *Bioact. Mater.*, 2024, **33**, 355–376.
3 Y. Li, Y. Han, X. Wang, J. Peng, Y. Xu and J. Chang, *ACS Appl. Mater. Interfaces*, 2017, **9**, 16054–16062.
4 S. H. Jeong, S. Cheong, T. Y. Kim, H. Choi and S. K. Hahn, *ACS Appl. Mater. Interfaces*, 2023, **15**, 16471–16481.
5 H. Zhong, Z. Chen, J. Huang, X. Yu, C. Wang, Y. Zheng, M. Peng and Z. Yuan, *J. Mater. Chem. B*, 2025, **13**, 4819–4829.
6 T. Zhou, K. Zheng, B. Sui, A. R. Boccaccini and J. Sun, *Int. J. Biol. Macromol.*, 2020, **163**, 1938–1946.
7 L. Fan, H. Wu, X. Zhou, M. Peng, J. Tong, W. Xie and S. Liu, *Carbohydr. Polym.*, 2014, **105**, 253–259.

View Article Online
DOI: 10.1039/D5TB00919G

8 M. Wang, J. Li, W. Li, Z. Du and S. Qin, *Int. J. Biol. Macromol.*, 2018, **118**, 41–48.

9 Y. Zhang, M. Jiang, Y. Zhang, Q. Cao, X. Wang, Y. Han, G. Sun, Y. Li and J. Zhou, *Mater. Sci. Eng. C*, 2019, **104**, 110002.

10 M. Bercea, 2024, DOI: 10.3390/polym16142021.

11 F. Yokoyama, I. Masada, K. Shimamura, T. Ikawa and K. Monobe, *Colloid Polym. Sci.*, 1986, **264**, 595–601.

12 C. Luo, M. Huang, X. Sun, N. Wei, H. Shi, H. Li, M. Lin and J. Sun, *ACS Appl. Mater. Interfaces*, 2022, **14**, 2638–2649.

13 M. D. Figueroa-Pizano, I. Vélaz and M. E. Martínez-Barbosa, *J. Vis. Exp.*, 2019, **2020**, 1–9.

14 J. Chen, J. He, Y. Yang, L. Qiao, J. Hu, J. Zhang and B. Guo, *Acta Biomater.*, 2022, **146**, 119–130.

15 H. Chen, T. Li, M. Bilal, C. Cao, P. Zhao, X. Zhou, L. Yu, Q. Huang and L. Cao, *J. Agric. Food Chem.*, 2023, **71**, 16521–16532.

16 H. Li, Y. Li, Y. Wang, L. Liu, H. Dong, C. Zhang and T. Satoh, *Eur. Polym. J.*, 2023, **182**, 111719.

17 A. Maleki, A.-L. Kjøniksen and B. Nyström, *Carbohydr. Res.*, 2007, **342**, 2776–2792.

18 X. Han, L. S. Ju and J. Irudayaraj, *Mol. Pharm.*, 2023, **20**, 3338–3355.

19 C. Holzwarth, M. Vaegler, F. Gieseke, S. M. Pfister, R. Handgretinger, G. Kerst and I. Müller, *BMC Cell Biol.*, 2010, **11**, 11.

20 S. Khorshidi and A. Karkhaneh, *Mater. Sci. Eng. C*, 2021, **118**, 111522.

21 Y. He, Q. Chang and F. Lu, *Mater. Today Bio*, 2023, **20**, 100687.

22 S. R. Thom, *J. Appl. Physiol.*, 2009, **106**, 988–995.

23 M. Mozafari and M. E. Barbati, *Drug Discov. Today*, 2024, **29**, 104135.

24 S. Suvarnapathaki, X. Wu, D. Lantigua, M. A. Nguyen and G. Camci-Unal, *NPG Asia Mater.*, 2019, **11**, 65.

25 Y. Huang, Z. Fu, H. Wang, Z. Liu, M. Gao, Y. Luo, M. Zhang, J. Wang and D. Ni, *Adv. Sci.*, 2024, **11**, 2404813.

26 H. Shen, Y. Ma, C. Zhang, Y. Qiao, J. Chen and F. Sun, *ACS Appl. Nano Mater.*, 2024, **7**, 15171–15184.

27 X. Wu, X. Han, Y. Guo, Q. Liu, R. Sun, Z. Wen and C. Dai, DOI:doi:10.1515/rams-2022-0308.

28 P. Ghaffari-Bohlouli, H. Alimoradi, D. Freitas Siqueira Petri, S. Moghassemi, C. A. Amorim, L. Nie and A. Shavandi, *Chem. Eng. J.*, 2023, **473**, 145072.

29 D. Job, J. Matta, C.-T. Dang, Y. Raphael, J. Vorstenbosch, B. Helli, G. Merle and J. Barralet, *MedComm – Biomater. Appl.*, 2024, **3**, e75.

30 H. Joodaki and M. B. Panzer, *Proc. Inst. Mech. Eng. Part H J. Eng. Med.*, 2018, **232**, 323–343.

31 S. Suvarnapathaki, X. Wu, T. Zhang, M. A. Nguyen, A. A. Goulopoulos, B. Wu and G. Camci-Unal, *Bioact. Mater.*, 2022, **13**, 64–81.

32 J. Han, T. Lei and Q. Wu, *Cellulose*, 2013, **20**, 2947–2958.

33 R. W. Korsmeyer, R. Gurny, E. Doelker, P. Buri and N. A. Peppas, *Int. J. Pharm.*, 1983, **15**, 25–35.

34 C. Guo, Z. Zeng, S. Yu, X. Zhou, Q. Liu, D. Pei, D. Lu and Z. Geng, *J. Polym. Res.*, 2021, **28**, 417.

35 L. F. de Lima, A. L. Ferreira, G. H. M. do Nascimento, L. P. Cardoso, M. B. de Jesus and W. R. de Araujo, *Chem. Eng. J.*, 2024, **494**, 152885.

36 M. Ruffo, O. I. Parisi, M. Dattilo, F. Patitucci, R. Malivindi, V. Pezzi, T. Tzanov and F. Puoci, *Drug Deliv. Transl. Res.*, 2022, **12**, 1881–1894.

37 W. Strober, *Curr. Protoc. Immunol.*, 2015, **111**, A3.B.1-A3.B.3.

38 M. Piccioni, R. Peila, A. Varesano and C. Vineis, 2023, DOI: 10.3390/jfb14100524.

39 K. Guzińska, D. Kaźmierczak, M. Dymel, E. Pabjańczyk-Wlazło and M. Boguń, *Mater. Sci. Eng. C*, 2018, **93**, 800–808.

40 F. Fathurochman and M. I. Wuriantika, .

41 Y. Cheng, S. Lu, Z. Hu, B. Zhang, S. Li and P. Hong, *Int. J. Biol. Macromol.*, 2020, **164**, 3953–3964.

42 Y. Qin, J. Wang, C. Qiu, X. Xu and Z. Jin, *J. Agric. Food Chem.*, 2019, **67**, 3966–3980.

43 V. Enev, P. Sedláček, S. Jarábková, T. Velcer and M. Pekař, *Colloids Surfaces A Physicochem. Eng. Asp.*, 2019, **575**, 1–9.

44 Z. Z. Fu, S. J. Guo, C. X. Li, K. Wang, Q. Zhang and Q. Fu, *Phys. Chem. Chem. Phys.*, 2022, **24**, 1885–1895.

45 In *Infrared Spectroscopy: Fundamentals and Applications*, 2004, pp. 71–93.

46 S. Tanpichai, F. Phoothong and A. Boonmahitthisud, *Sci. Rep.*, 2022, **12**, 8920.

47 J. Wang, W. Wu and Z. Lin, *J Appl Polym Sci*, 2008, **109**, 3018–3023.

48 X. Ming, D. Zhang, H. Zhu, Q. Zhang and S. Zhu, *Adv. Funct. Mater.*, 2024, **34**, 2411560.

49 S. Noguchi and K. Takaomi, *Ultrason. Sonochem.*, 2020, **67**, 105143.

50 C. Wang, Z. Shen, P. Hu, T. Wang, X. Zhang, L. Liang, J. Bai, L. Qiu, X. Lai, X. Yang and K. Zhang, *J. Sol-Gel Sci. Technol.*, 2022, **101**, 103–113.

51 F. H. Falqi, O. A. Bin-Dahman, M. Hussain and M. A. Al-Harthi, *Int. J. Polym. Sci.*, 2018, **2018**, 8527693.

52 Y. Ben Azaza, A. van der lee, S. Li, M. Nasri and R. Nasri, *Sustain. Chem. Pharm.*, 2023, **31**, 100905.

53 A. S. Wadajkar, C. Ahn, K. T. Nguyen, Q. Zhu and T. Komabayashi, *Int. Sch. Res. Not.*, 2014, **2014**, 191068.

54 S. Azzam, L. Tomasova, C. Danner, M. Skiba, M. Klein, Z. Guttenberg, S. Michaelis and J. Wegener, *Sci. Rep.*, 2024, **14**, 9103.

55 M. D'Urso and N. A. Kurniawan, *Front. Bioeng. Biotechnol.*, 2020, **8**, 609653.

56 W. Tiskratok, N. Chuinsiri, P. Limraksasin, M. Kyawsoewin and P. Jitprasertwong, 2025, DOI: 10.3390/polym17060822.

57 J. R. Landolph, *Am. J. Ind. Med.*, 1985, **7**, 31–43.

58 M. Ribeiro, M. Simões, C. Vitorino and F. Mascarenhas-Melo, *Gels (Basel, Switzerland)*, DOI:10.3390/gels10030188.

59 A. E. Morguette, G. Bartolomeu-Gonçalves, G. M. Andriani, G. E.

View Article Online
DOI: 10.1039/D5TB00919G

Bertoncini, I. M. Castro, L. F. Spoladori, A. M. Bertão, E. R. Tavares, L. M. Yamauchi and S. F. Yamada-Ogatta, 2023, DOI: 10.3390/plants12112147.

60 N. Sedighi-Pirsaraei, A. Tamimi, F. Sadeghi Khamaneh, S. Dadras-Jeddi and N. Javaheri, *Front. Bioeng. Biotechnol.*, 2024, **12**, 1–18.

View Article Online
DOI: 10.1039/D5TB00919G

Data availability

The data supporting this article have been included as part of the Supplementary Information.